Pulse Engineering via Projection of Response Functions

Nicolas Heimann, 1, 2, 3, * Lukas Broers, 1, 2 and Ludwig Mathey 1, 2, 3

¹ Zentrum für Optische Quantentechnologien, Universität Hamburg, 22761 Hamburg, Germany ² Institut für Quantenphysik, Universität Hamburg, 22761 Hamburg, Germany ³ The Hamburg Centre for Ultrafast Imaging, 22761 Hamburg, Germany

We present an iterative optimal control method of quantum systems, aimed at an implementation of a desired operation with optimal fidelity. The update step of the method is based on the linear response of the fidelity to the control operators, and its projection onto the mode functions of the corresponding operator. Our method extends methods such as gradient ascent pulse engineering and variational quantum algorithms, by determining the fidelity gradient in a hyperparameter-free manner, and using it for a multi-parameter update, capitalizing on the multi-mode overlap of the perturbation and the mode functions. This directly reduces the number of dynamical trajectories that need to be evaluated in order to update a set of parameters. We demonstrate this approach, and compare it to the standard GRAPE algorithm, for the example of a quantum gate on two qubits, demonstrating a clear improvement in convergence and optimal fidelity of the generated protocol.

Algorithmic control and optimized utilization of quantum computational devices plays a central role in the research of quantum technologies. In recent years, the emergent field of quantum machine learning has brought forth new optimization heuristics that expand the body of quantum optimal control (QOC) [1–3]. One key method is gradient ascent pulse engineering (GRAPE) [4, 5], which is a QOC method that is based on estimating gradients in a space of control parameters to navigate the error surface of a given objective. As such GRAPE has found utilization in the context of quantum computing [6–9]. Further, variational quantum algorithms (VQAs) [10, 11] provide a more recent circuit based approach to QOC [12–16] in the context of parameterized quantum circuits.

Gradient based optimization methods, such as GRAPE, rely on finite differences and large statistics in online utilization on quantum devices, both of which are prone to errors. The multitude of dynamic trajectories (or runs) that have to be realized either in the numerical simulation that is employed or on a real device, are a bottle-neck of gradient based heuristics [17, 18]. While VQAs are kept in high regard as a promising utilization of noisy intermediate-scale quantum (NISQ) devices [19, 20], they have been repeatedly shown to display serious shortcomings [21–24]. This has highlighted the necessity for extensions of VQA methods [23, 25–27].

In this paper, we demonstrate a pulse engineering method based on linear response functions of time-local perturbations for parameterizations of the Hamiltonian that are non-local in time. We refer to our method as pulse engineering via projection of response functions (PEPR). The objective of this method is to generate an implementation of a desired operation, such as a quantum algorithm, with optimal fidelity. We assume that the quantum system can be controlled via a set of control terms, composed of a set of operators and control

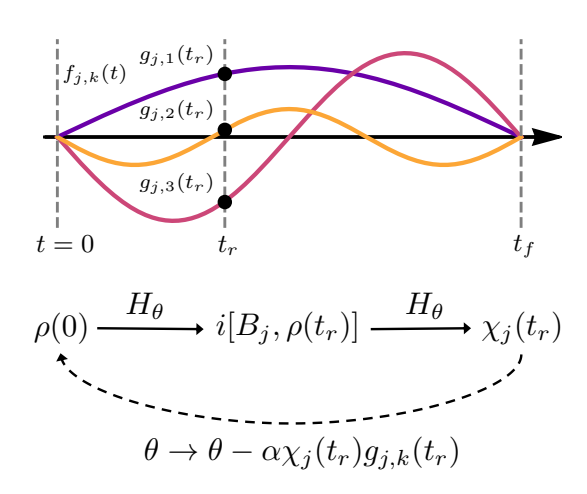


Figure 1. Illustration of the PEPR method. Panel (a) shows temporally non-local mode functions $f_{i,k}(t)$ of the control functions that parameterize the time-dependent Hamiltonian. The objective is to optimize the fidelity of a desired operation, which is done via iterative updates of the trainable parameters. These updates are based on the response to a perturbation at a random time t_r , and the projection of the response onto the mode function $f_{j,k}(t)$, which uses the projection coefficients $g_{j,k}(t_r)$. In panel (b) we display a single update schematically. The random initial state $\rho(0)$ is propagated to the random time t_r . The commutator with one of the control operators B_j is taken. Then, the resulting density operator is propagated to the time t_f , and the response function $\chi_i(t_r)$ is determined. This quantity, together with the projection coefficient $g_{i,k}(t_r)$ and a learning rate α , is used for the update.

functions. We expand each of these control functions into a set of mode functions, which have an arbitrary time dependence in general, and are temporally non-local, in particular. In each update step, we determine the response of the fidelity to one of the control operators. This generates the gradient of the fidelity in a hyperparameter-free manner. Next, we determine the optimal update of the control parameters via the projection of the response function on the modes of the control func-

^{*} nheimann@physnet.uni-hamburg.de

tions, resulting in a multi-parameter update. These key features of the method directly address the bottle-neck of growing parameter-spaces in gradient based methods, by reducing the necessary amount of dynamical trajectories to iterate over parameter updates. Another advantage is the above mentioned elimination of a hyperparameter associated with finite difference methods, improving the usability in a practical setting.

This method can be generally applied to conjugate sets of mode functions of the control functions for the perturbation and the parameterization to maximize the projection coefficients. Here, we opt for a time-local perturbation and consequently a temporally non-local parameterization based on Fourier modes [27]. We consider this approach to be an extension of GRAPE-like methods and VQAs that utilizes non-local parameterizations in an efficient manner and addresses common issues, such as gradient estimation and scaling-behavior of gradient based methods.

We compare the performance of PEPR to that of standard GRAPE in a minimal example of compiling an entangling gate on two qubits. As we discuss below, we find that both the fidelity of the generated protocol, as well as the convergence towards this protocol, is improved in a convincing fashion. We note that QOC has been related to linear response theory in [28].

The method works as follows, see Fig. 1 for an illustration. Analogously to variational and optimal control approaches, we consider a Hamiltonian of the form

$$H_{\theta} = H_0 + \sum_{j=1}^{n_B} \theta_j(t) B_j.$$
 (1)

The control operators B_j represent the options of external control of the system, with n_B being the number of them. We write general parameterizations of the time-dependent control functions $\theta_j(t)$ as

$$\theta_j(t) = \sum_{k=1}^{n_j} \theta_{j,k} f_{j,k}(t),$$
(2)

where $\theta_{j,k}$ are parameters, and $f_{j,k}(t)$ are mode functions of the control functions of the parameterization. The term H_0 in Eq. 1 is the part of the Hamiltonian that can not be controlled externally.

We use this Hamiltonian to propagate an initial density matrix $\rho(0)$ over the time interval of $t \in [0, t_f]$, such that we obtain the density operator $\rho(t_f)$. The objective of the

algorithm is to maximize the fidelity of the state $\rho(t_f)$, compared to the target state that a target transformation V produces, i.e. $\rho^* = V \rho(0) V^{\dagger}$. We therefore write the state-fidelity as

$$F_{\theta}(\rho) = \operatorname{Tr}(\rho(t_f)\rho^*),$$
 (3)

where the subscript θ emphasizes the dependence on the parameters which determine the time-evolution that produces $\rho(t_f)$. Equivalently, we aim to minimize the infidelity $1-F_{\theta}(\rho)$ for any initial state $\rho(0)$. For this purpose, we approach an optimal or near-optimal implementation in an iterative fashion.

Next, we consider a perturbation of the system of the form

$$H_p = -\epsilon \delta(t - t_r) B_j. \tag{4}$$

The perturbation occurs at time t_r , with the time-dependence of a δ -function. B_j is one of the control operators via which the system can be controlled as presented in Eq. 1. The prefactor ϵ is utilized as a perturbative expansion parameter. We choose the time randomly in the interval $t_r \in [0, t_f]$, and we choose the operator B_j randomly, via a random choice of the index $j = 1, \ldots, n_B$.

We then follow the standard result of linear response theory, in which the change of the expectation value of an observable A, due to a perturbation of the form $H_p = -F(t)B$ is of the general form

$$\Delta \langle A \rangle = \int_{-\infty}^{\infty} dt' \chi_{AB}(t, t') F(t') \tag{5}$$

with the susceptibility

$$\chi_{AB}(t,t') = \frac{i}{\hbar} \Theta(t-t') \langle [A_I(t), B_I(t')] \rangle, \qquad (6)$$

where $A_I(t)$ and $B_I(t')$ are the operators A and B in the interaction picture, respectively.

We apply this approach to the optimization objective mentioned above. In this context, the observable A is the target state ρ^* . The time at which this observable is evaluated is t_f , such that we have $A_I(t_f) = U^{\dagger}(t_f)\rho^*U(t_f)$, where $U(t_f) = U(0, t_f)$ is the time-evolution operator from time 0 to time t_f . The perturbation contains one of the control operators B_j , and $F(t) = \epsilon \delta(t - t_r)$. We therefore have $B_{j,I}(t_r) = U^{\dagger}(t_r)B_jU(t_r)$. With this, we write

$$\chi_{j}(t_{r}) \equiv \chi_{F_{\theta},B_{j}}(t_{f},t_{r}) = \frac{i}{\hbar} \operatorname{Tr} \left(\left[U^{\dagger}(t_{f})\rho^{*}U(t_{f}), U^{\dagger}(t_{r})B_{j}U(t_{r}) \right] \rho(0) \right)$$

$$= \frac{i}{\hbar} \operatorname{Tr} \left(\rho^{*}U(t_{r},t_{f}) \left[B_{j}, U(t_{r})\rho(0)U^{\dagger}(t_{r}) \right] U^{\dagger}(t_{r},t_{f}) \right),$$

$$(8)$$

where we note that $t_f > t_r$, such that $\Theta(t_f - t_r) = 1$. Furthermore, using Eq. 5 and $F(t) = \epsilon \delta(t - t_r)$, we obtain

$$\frac{\Delta F_{\theta}}{\epsilon} = \chi_j(t_r). \tag{9}$$

This expression shows that the gradient of the fidelity in the operator space spanned by the control operators B_j , is determined by computing the linear response of the fidelity with regard to that operator at a time t_r .

Based on this response function, we determine the optimal update of the parameters $\theta_{j,k}$ as follows, where the index j corresponds to the operator B_j in Eq. 4. We write the projection of the δ -function that is used in the perturbation in Eq. 4 onto the mode functions of the control functions of the parameterization as

$$\delta(t - t_r) = \sum_{k=1}^{\infty} g_{j,k}(t_r) f_{j,k}(t).$$
 (10)

The $g_{j,k}(t)$ are conjugate functions to the $f_{j,k}(t)$ in the sense of a decomposition of the δ -function. Based on this decomposition of the time dependence of the perturbation in terms of the mode functions of the control function of the control operator B_j , we obtain the update rule

$$\theta_{j,k} \rightarrow \theta_{j,k} - \alpha_0 g_{j,k}(t_r) \chi_j(t_r),$$
 (11)

where we introduce the parameter α_0 , which in similar contexts is referred to as a learning rate or step size. While the decomposition in Eq. 10 is exact, we use the approximation of truncating the sum by the number of modes n_i that are included in the representation in Eq. 2. With this, we identify the term $-\alpha_0 g_{j,k}(t_r) \chi_j(t_r)$ as a correction to the parameters $\theta_{j,k}$. We emphasize that $\chi_i(t_r)$ in Eq. 11 is used to update n_j -many parameters $\theta_{j,k}$ without increasing the numerical complexity of the approach, assuming that the corresponding $g_{i,k}(t_r) \neq 0$. This is in contrast to conventional variational methods, in which the complexity grows with the controllability of the Hamiltonian. Therefore, this method directly benefits from parameterizations in which the mode functions of the control functions have significant overlap with the time dependence of the perturbation, i.e. the δ -functions acting at different times.

Note that $\theta_j(t)$ are functions that can be arbitrarily parameterized through choices of $f_{j,k}(t)$ in Eq. 2. Common parameterizations in optimal control contexts use time-local step-wise functions, which is adjacent to parameterized variational quantum circuit methods, or low-dimensional random bases [29, 30]. Since this method is an extension of GRAPE, and relies on, and benefits from, the overlap between different functional bases for the perturbation and the parameterization of the Hamiltonian, we refer to it as pulse engineering via the projection of response functions (PEPR). Hence, a central aspect of PEPR is the overlap of parameterization mode functions of the control functions and the perturbation mode functions of the control functions.

As an example that implements these considerations, we choose the temporally non-local parameterization of Fourier modes [27], which consists of mode functions of the control functions that all have overlap with (almost)

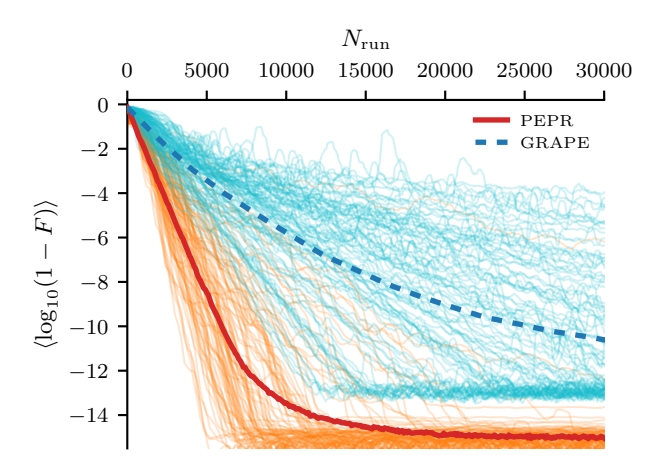


Figure 2. PEPR vs GRAPE. The average infidelity $\langle \log_{10}(1-F) \rangle$, as a function of the number of runs N_{run} , obtained using PEPR (red line) and GRAPE (blue dashed). The underlying ensembles of realizations $\{1 - F_{\theta}\}$ for PEPR and GRAPE are depicted as orange and cyan lines, respectively. PEPR leads to faster convergence with a reduced variance of the underlying realizations, compared to GRAPE. Furthermore, the infidelity that is achieved is consistently smaller for PEPR than for GRAPE. In this example, we compare $n_i = 8$ modes and use an individual set of optimal hyperparameters for each method: $\alpha_{PEPR} = 0.5$, $\alpha_{GRAPE} = 1.2$ and $\epsilon = 10^{-7}$. The lower bound of the average infidelity is determined by the accuracy of the used numerical method. Here we use 4thorder Runge-Kutta with a time-discretization of $h = 2^{-14}$. Due to the additional error of the gradient estimate, this is more detrimental for GRAPE.

any time-local perturbation proportional to $\delta(t-t')$. This particular parameterization is

$$\theta_j(t) = \sum_{k=1}^{n_j} \theta_{j,k} \sin\left(\pi k \frac{t}{t_f}\right). \tag{12}$$

This means that the decomposition of the δ -function in Eq. 10 is now given through the functions

$$f_{j,k}(t) = \sin\left(\pi k \frac{t}{t_{\rm f}}\right) \tag{13}$$

$$g_{j,k}(t) = \frac{2}{t_{\rm f}} \sin\left(\pi k \frac{t}{t_{\rm f}}\right),\tag{14}$$

such that we obtain the update rule

$$\theta_{j,k} \rightarrow \theta_{j,k} - \alpha \sin\left(\pi k \frac{t_r}{t_f}\right) \chi_j(t_r),$$
 (15)

where we have introduced the effective learning rate $\alpha = \alpha_0 \frac{2}{t_e}$.

We demonstrate PEPR for a simple example of the target transformation $V={\rm CNOT}$ on two qubits. The full Hamiltonian reads

$$H(t) = \sum_{j=1}^{2} h_{x,j}(t)\sigma_{x}^{j} + h_{y,j}(t)\sigma_{y}^{j} + J(t)\vec{\sigma}^{1}\vec{\sigma}^{2},$$
 (16)

where $\vec{\sigma}$ is the vector of Pauli matrices. The time-dependent functions are equivalent to the $\theta_j(t)$ in Eq. 2. We parameterize these functions as described in Eq. 12 such that

$$h_{x/y,j}(t) = \sum_{k=1}^{n_j} \theta_{x/y,j,k} \sin\left(\pi k \frac{t}{t_f}\right)$$
 (17)

$$J(t) = \sum_{k=1}^{n_j} \theta_{J,k} \sin\left(\pi k \frac{t}{t_f}\right). \tag{18}$$

We begin by randomly sampling the initial parameters θ from normal distributions, i.e. $\theta_{j,k} \sim \mathcal{N}(0,1)$. We then follow the PEPR procedure, described above, to iteratively update these parameters in order to identify parameters that produce a time-evolution that implements the target transformation V. In each iteration, we initialize the state of the system in a product state $\rho(0) = \rho_1 \otimes \rho_2$, where ρ_1 and ρ_2 are random local pure states, see App. B, for details. We randomly choose the control operator $B_j \in \{\sigma_x^1, \sigma_y^1, \sigma_x^2, \sigma_y^2, \vec{\sigma}^1 \vec{\sigma}^2\}$ and evaluate the susceptibility $\chi_j(t_r)$ for a random time $t_r \in [0, t_f]$. We then update the parameters according to Eq. 15.

Up to this point, we have described a method that operates using a state-fidelity. By averaging over these fidelities we obtain a metric that is representative of the fidelity of the unitary transformation realized through the time-evolution. We therefore approximate the infidelity of the transformation by considering n_F trajectories $\{\rho\}$, obtained from different initial states $\rho(0)$, and averaging over their state-fidelities, such that

$$1 - F_{\theta} = 1 - \frac{1}{n_F} \sum_{\{\rho\}} F_{\theta}(\rho). \tag{19}$$

 $F_{\theta}(\rho)$ is the state-fidelity according to Eq. 3, where the subscript emphasizes the dependence on the parameters θ . Here we choose an empirical sampling size of $n_F = 10$. The result of this method, as well as similar optimization approaches, is intrinsically probabilistic. In particular, the random initial parameters θ are the starting point for the local optimization sequence within the parameter space. In order to present a meaningful comparison, we show many realizations of this algorithm with n_T different initial parameters $\{\theta\}$. We also show the average infidelity over this ensemble of optimization trajectories. We write

$$\langle \log_{10}(1-F)\rangle = \frac{1}{n_T} \sum_{\{\theta\}} \log_{10}(1-F_{\theta}).$$
 (20)

Here we choose an empirical sampling size of $n_T = 100$. Note that this is the log-mean of the infidelity, which gives higher weight to low-infidelity realizations. We choose this more involved average as visual support for the set of trajectories in Fig. 2, see below.

We demonstrate our method in the case of the target transformation of the CNOT gate. As a compara-

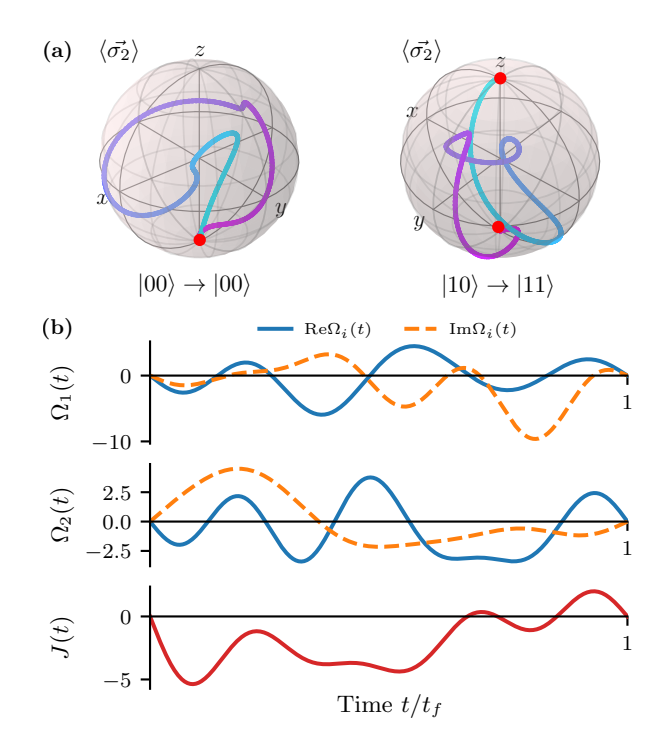


Figure 3. **PEPR** based high-fidelity protocol. In panel (a) we show the time-evolution of the Bloch vector of the target qubit $\langle \vec{\sigma} \rangle$ under a high-fidelity implementation of the CNOT transformation for $|00\rangle \rightarrow |00\rangle$ and $|10\rangle \rightarrow |11\rangle$. The time t is depicted as the line color and the initial and final states are depicted as red dots. In panel (b) we show the corresponding control functions $\Omega_i(t) = h_{x,i}(t) - ih_{y,i}(t)$ and J(t). We note that the amplitudes $|\Omega_i(t)|$ and J(t) are within reasonable boundaries for the given energy scales of the system, defined by the final time t_f .

tive benchmark, we additionally optimize the parameters based on the GRAPE method, see App. A for details. In the version of GRAPE used here, we update all the parameters in a single iteration. Therefore, GRAPE requires calculating $5n_i + 1$ time-evolutions to estimate the gradient of the infidelity in a single iteration. We emphasize this with regards to our definition of the number of runs $N_{\rm run}$, which is the number of calculated timeevolutions during a sequence of parameter updates. In Fig. 2 we show results of the optimization using both PEPR and GRAPE. We use an optimized set of hyperparameters $\alpha_{\text{PEPR}} = 0.5$, $\alpha_{\text{GRAPE}} = 1.2$ and $\epsilon = 10^{-7}$ for each method to provide an unbiased comparison, as discussed in App. B. The optimization trajectories generated using PEPR converge faster to low values of the infidelity and show a reduced variance for a given number of runs $N_{\rm run}$, compared to GRAPE. The lower bound is determined by the accuracy of the numerical integration method. Here, we use standard 4th-order Runge-Kutta with a time-discretization of $h = 2^{-14}t_f$. The lower bound of the optimization trajectories using GRAPE additionally depends on the finite difference length ϵ . Note that the standard GRAPE results show a large variance in the quality of optimization trajectories, compared to

PEPR, where we more reliably find fast-converging high-fidelity solutions. The average infidelity over the ensemble of optimization trajectories $\langle \log_{10}(1-F) \rangle$ also reflects this convergence behavior.

We show an example for a high-fidelity implementation of the CNOT gate generated via PEPR in Fig. 3. We show the time-evolution of the Bloch-vector of the target qubit $\langle \vec{\sigma}^2(t) \rangle = (\langle \sigma_x^2(t) \rangle, \langle \sigma_y^2(t) \rangle, \langle \sigma_z^2(t) \rangle)^T$ for the example of the initial states $|00\rangle$ and $|10\rangle$. The trajectory of $\langle \vec{\sigma}^2(t) \rangle$ is continuous and efficient on the time scale of t_f . We note that the amplitudes of the control functions are within reasonable boundaries, resulting in a realistic protocol.

In conclusion, we have presented a quantum optimization method based on linear response theory, and further based on projecting the response onto control parameters. Maximizing these projection coefficients results in a more efficient update rule that drastically reduces the number of dynamical realizations of the time-evolution necessary to update a set of parameters. Due to the nature of our approach, we refer to it as pulse engineering via the projection of response functions (PEPR). We understand this method in the context of the current resurgence of quantum optimal control theory under the moniker of quantum machine learning. PEPR is adjacent to GRAPE and VQAs, but extends them efficiently

to time-non-local parameterizations, that directly benefit from the projection feature of the method. In the endeavor to maximize the overlap of perturbation and parameterization bases, we consider a parameterization that utilizes the low-frequency Fourier mode expansion.

In a minimal proof-of-concept example we demonstrate the benefits of PEPR over standard GRAPE. In a direct comparison of optimizing the CNOT gate, we find that PEPR produces high-fidelity solutions more reliably. Importantly, PEPR is more efficient in its optimization as it consistently requires less evaluations of time-evolution trajectories in order to optimize its protocols. The evaluation of such time-evolutions in order to navigate the parameter space is an important bottleneck of gradient based methods. Therefore, this improvement of quantum optimal control methods will support the design and establishment of quantum technology going forward.

ACKNOWLEDGMENTS

This work is funded by the Deutsche Forschungs-gemeinschaft (DFG, German Research Foundation) - SFB-925 - project 170620586 and the Cluster of Excellence 'Advanced Imaging of Matter' (EXC 2056) project 390715994.

- A. P. Peirce, M. A. Dahleh, and H. Rabitz, Optimal control of quantum-mechanical systems: Existence, numerical approximation, and applications, Phys. Rev. A 37, 4950 (1988).
- [2] C. Brif, R. Chakrabarti, and H. Rabitz, Control of quantum phenomena: past, present and future, New Journal of Physics 12, 075008 (2010).
- [3] C. Koch, U. Boscain, T. Calarco, G. Dirr, S. Filipp, S. Glaser, R. Kosloff, S. Montangero, T. Schulte-Herbrueggen, D. Sugny, and F. Wilhelm, Quantum optimal control in quantum technologies. strategic report on current status, visions and goals for research in europe, EPJ Quantum Technology 9 (2022).
- [4] J. P. Palao and R. Kosloff, Optimal control theory for unitary transformations, Phys. Rev. A 68, 062308 (2003).
- [5] N. Khaneja, T. Reiss, C. Kehlet, T. Schulte-Herbrüggen, and S. J. Glaser, Optimal control of coupled spin dynamics: design of NMR pulse sequences by gradient ascent algorithms, Journal of Magnetic Resonance 172, 296 (2005).
- [6] P. Rebentrost and F. K. Wilhelm, Optimal control of a leaking qubit, Phys. Rev. B 79, 060507 (2009).
- [7] D. J. Egger and F. K. Wilhelm, Optimized controlled-z gates for two superconducting qubits coupled through a resonator, Superconductor Science and Technology 27, 014001 (2013).
- [8] S. Jandura and G. Pupillo, Time-Optimal Two- and Three-Qubit Gates for Rydberg Atoms, Quantum 6, 712 (2022).
- [9] N. Heimann, L. Broers, N. Pintul, T. Petersen, K. Sponselee, A. Ilin, C. Becker, and L. Mathey, Quantum

- gate optimization for rydberg architectures in the weak-coupling limit (2023), arXiv:2306.08691 [quant-ph].
- [10] J. R. McClean, J. Romero, R. Babbush, and A. Aspuru-Guzik, The theory of variational hybrid quantum-classical algorithms, New Journal of Physics 18, 023023 (2016).
- [11] M. Cerezo, A. Arrasmith, R. Babbush, S. C. Benjamin, S. Endo, K. Fujii, J. R. McClean, K. Mitarai, X. Yuan, L. Cincio, and P. J. Coles, Variational quantum algorithms, Nature Reviews Physics 3, 625 (2021).
- [12] J. Li, X. Yang, X. Peng, and C.-P. Sun, Hybrid quantumclassical approach to quantum optimal control, Phys. Rev. Lett. 118, 150503 (2017).
- [13] A. Choquette, A. Di Paolo, P. K. Barkoutsos, D. Sénéchal, I. Tavernelli, and A. Blais, Quantumoptimal-control-inspired ansatz for variational quantum algorithms, Phys. Rev. Res. 3, 023092 (2021).
- [14] A. B. Magann, C. Arenz, M. D. Grace, T.-S. Ho, R. L. Kosut, J. R. McClean, H. A. Rabitz, and M. Sarovar, From pulses to circuits and back again: A quantum optimal control perspective on variational quantum algorithms, PRX Quantum 2, 010101 (2021).
- [15] O. R. Meitei, B. T. Gard, G. S. Barron, D. P. Pappas, S. E. Economou, E. Barnes, and N. J. Mayhall, Gate-free state preparation for fast variational quantum eigensolver simulations, npj Quantum Information 7, 155 (2021).
- [16] R. de Keijzer, O. Tse, and S. Kokkelmans, Pulse based Variational Quantum Optimal Control for hybrid quantum computing, Quantum 7, 908 (2023).
- [17] L. Bittel, J. Watty, and M. Kliesch, Fast gradient estimation for variational quantum algorithms (2022),

- arXiv:2210.06484 [quant-ph].
- [18] D. Wierichs, J. Izaac, C. Wang, and C. Y.-Y. Lin, General parameter-shift rules for quantum gradients, Quantum 6, 677 (2022).
- [19] J. Preskill, Quantum Computing in the NISQ era and beyond, Quantum 2, 79 (2018).
- [20] K. Bharti, A. Cervera-Lierta, T. H. Kyaw, T. Haug, S. Alperin-Lea, A. Anand, M. Degroote, H. Heimonen, J. S. Kottmann, T. Menke, W.-K. Mok, S. Sim, L.-C. Kwek, and A. Aspuru-Guzik, Noisy intermediate-scale quantum algorithms, Rev. Mod. Phys. 94, 015004 (2022).
- [21] J. R. McClean, S. Boixo, V. N. Smelyanskiy, R. Babbush, and H. Neven, Barren plateaus in quantum neural network training landscapes, Nature Communications 9, 4812 (2018).
- [22] L. Bittel and M. Kliesch, Training variational quantum algorithms is np-hard, Phys. Rev. Lett. 127, 120502 (2021).
- [23] Z. Holmes, K. Sharma, M. Cerezo, and P. J. Coles, Connecting ansatz expressibility to gradient magnitudes and barren plateaus, PRX Quantum 3, 010313 (2022).
- [24] E. R. Anschuetz and B. T. Kiani, Quantum variational algorithms are swamped with traps, Nature Communica-

- tions 13, 7760 (2022).
- [25] E. Grant, L. Wossnig, M. Ostaszewski, and M. Benedetti, An initialization strategy for addressing barren plateaus in parametrized quantum circuits, Quantum 3, 214 (2019).
- [26] M. Cerezo, A. Sone, T. Volkoff, L. Cincio, and P. J. Coles, Cost function dependent barren plateaus in shallow parametrized quantum circuits, Nature Communications 12, 1791 (2021).
- [27] L. Broers and L. Mathey, Mitigated barren plateaus in the time-nonlocal optimization of analog quantumalgorithm protocols, Phys. Rev. Res. 6, 013076 (2024).
- [28] A. Castro and I. V. Tokatly, Quantum optimal control theory in the linear response formalism, Phys. Rev. A 84, 033410 (2011).
- [29] P. Doria, T. Calarco, and S. Montangero, Optimal control technique for many-body quantum dynamics, Phys. Rev. Lett. 106, 190501 (2011).
- [30] T. Caneva, T. Calarco, and S. Montangero, Chopped random-basis quantum optimization, Phys. Rev. A 84, 022326 (2011).

Appendix A: Gradient Ascent Pulse Engineering

The objective of GRAPE [5] is to minimize a certain loss function defined for a quantum system by inferring an optimal set of parameters θ_{opt} that define the dynamics of that system. Here, we consider the Hamiltonian H_{θ} in Eq. 1, which produces the formal time-evolution operator

$$U_{\theta}(0, t_f) = e^{-\frac{i}{\hbar} \int_0^{t_f} H_{\theta}(t)dt}.$$
 (A1)

There are various ways to construct a loss function to evaluate the dynamics with. For instance, given a target transformation V, we can define the state-infidelity

$$1 - F = \text{Tr}(V\rho_0 V^{\dagger} \rho(t_f)), \tag{A2}$$

where ρ_0 is some initial state and $\rho(t_f) = U(0, t_f)\rho_0 U^{\dagger}(0, t_f)$ is the state obtained from time-propagating the initial state ρ_0 from the initial time t = 0 to t_f . The central idea behind GRAPE is to update the parameters θ by gradient ascent (or descent) with respect to the loss function \mathcal{L} . It is possible to approximate the gradient of the loss function $\nabla \mathcal{L}$ by the finite differences

$$\frac{\partial \mathcal{L}}{\partial \theta_{ik}} = \frac{\mathcal{L}(\theta + e_{kj}\epsilon) - \mathcal{L}(\theta)}{\epsilon},\tag{A3}$$

where $e_{j,k}$ is the unit-vector corresponding to the parameter $\theta_{j,k}$. This allows us to update the parameters as

$$\theta \to \theta - \alpha \nabla \mathcal{L}.$$
 (A4)

 α is a hyperparameter commonly reffered to as the learning rate in gradient descent contexts. We note that rather than utilizing the full gradient, the parameters $\theta_{j,k}$ can also be updated individually. This requires two evaluation of the loss function per parameter, i.e. $\mathcal{L}(\theta_{j,k}+\epsilon)$ and $\mathcal{L}(\theta_{j,k})$. Therefore, it is common to update all the parameters within a single iteration of the update rule. This reduces the computational costs from $2|\theta|$ to $|\theta|+1$ time-evolutions, where $|\theta|$ is the number of parameters.

Appendix B: CNOT Gate

In this section we describe the model we use in the main-text to demonstrate the performance of PEPR to obtain high-fidelity realizations of the CNOT gate. The qubits are locally controlled as

$$H_1(t) = h_{x,1}(t)\sigma_x^1 + h_{y,1}(t)\sigma_y^1,$$
(B1)

$$H_2(t) = h_{x,2}(t)\sigma_x^2 + h_{y,2}(t)\sigma_y^2,$$
(B2)

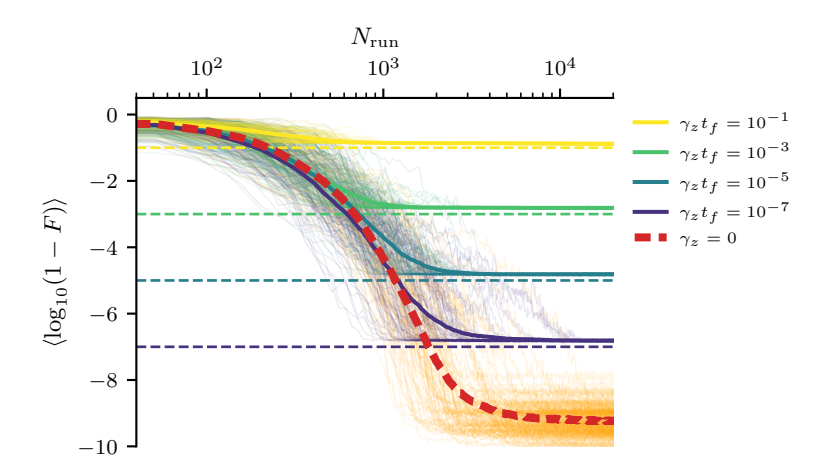


Figure 4. Results of PEPR for the CNOT gate. The average infidelity $\langle \log_{10}(1-F) \rangle$, as a function of the number of runs N_{run} , for different rates of dissipation γ_z , with $n_j = 8$ and $\alpha_{\text{PEPR}} = 0.4$. The corresponding ensembles of realizations $\{1 - F_l\}_{\gamma_z}$ are depicted as thin lines. The estimated lower bounds $\gamma_z t_f$ of the infidelity are depicted as dashed lines. Without dissipation, the lower bound of the infidelity is determined by the time-discretization h of the 4th-order Runge-Kutta method.

where $\sigma_j^1 = \sigma_j \otimes 1$, and $\sigma_j^2 = 1 \otimes \sigma_j$ are the local Pauli matrices. The interaction-term between the qubits is

$$H_{\rm int} = J(t)\vec{\sigma}_1\vec{\sigma}_2,\tag{B3}$$

where $\vec{\sigma}_1\vec{\sigma}_2 = \sigma_x \otimes \sigma_x + \sigma_y \otimes \sigma_y + \sigma_z \otimes \sigma_z$, and J(t) is the time-dependent strength of the interaction. We write the resulting Hamiltonian as

$$H_{\theta} = H_{1} + H_{2} + H_{\text{int}} = \begin{pmatrix} J & h_{x,2} - ih_{y,2} & h_{x,1} - ih_{y,1} & 0\\ h_{x,2} + ih_{y,2} & -J & 2J & h_{x,1} - ih_{y,1}\\ h_{x,1} + ih_{y,1} & 2J & -J & h_{x,2} - ih_{y,2}\\ 0 & h_{x,1} + ih_{y,1} & h_{x,2} + ih_{y,2} & J \end{pmatrix}.$$
 (B4)

As outlined in the main-text, we consider the parameterized protocols

$$h_{p,i}(t) = \sum_{k} \theta_{p,i,k} \sin\left(\pi k \frac{t}{t_f}\right)$$
 (B5)

$$J(t) = \sum_{k} \theta_{J,k} \sin\left(\pi k \frac{t}{t_f}\right),\tag{B6}$$

where $p \in \{x, y\}$, $i \in \{1, 2\}$. We explicitly write the density operator of the system as

$$\rho = \begin{pmatrix}
\rho_1 & \rho_4 - i\rho_5 & \rho_6 - i\rho_7 & \rho_{10} - i\rho_{11} \\
\rho_4 + i\rho_5 & \rho_2 & \rho_8 - i\rho_9 & \rho_{12} - i\rho_{13} \\
\rho_6 + i\rho_7 & \rho_8 + i\rho_9 & \rho_3 & \rho_{14} - i\rho_{15} \\
\rho_{10} + i\rho_{11} & \rho_{12} + i\rho_{13} & \rho_{14} + i\rho_{15} & \xi - \rho_1 - \rho_2 - \rho_3
\end{pmatrix}.$$
(B7)

where $\rho_i \in \mathbb{R}$, and $\xi \in \{0,1\}$ defines the value of trace of the state. We note that $\xi = 0$ is required to time-propagate $i[B_j, \rho]$, as $\text{Tr}([B_j, \rho]) = 0$. For numerical purpose, we choose to represent ρ as a real-valued vector

$$\vec{\rho} = (\rho_1, ..., \rho_{15})^T.$$
 (B8)

We include dissipation in the form of pure-dephasing of the individual qubits. The time-evolution of the state is governed by the Lindblad master equation

$$\frac{\partial \rho}{\partial t} = -\frac{i}{\hbar} [H_{\theta}(t), \rho] + \gamma_z \sum_{i} \mathcal{D}[\sigma_z^i] \rho, \tag{B9}$$

where $\mathcal{D}[L]\rho = L\rho L^{\dagger} - \frac{1}{2}\{L^{\dagger}L, \rho\}$. The equations of motion read

$$\partial_t \rho_1 = 2(-h_{y,2}\rho_4 + h_{x,2}\rho_5 - h_{y,1}\rho_6 + h_{x,1}\rho_7) \tag{B10}$$

$$\partial_t \rho_2 = 2(-h_{v,1}\rho_{12} + h_{x,1}\rho_{13} + h_{v,2}\rho_4 - h_{x,2}\rho_5 + 2J\rho_9) \tag{B11}$$

$$\partial_t \rho_3 = -2(h_{y,2}\rho_{14} - h_{x,2}\rho_{15} - h_{y,1}\rho_6 + h_{x,1}\rho_7 + 2J\rho_9) \tag{B12}$$

$$\partial_t \rho_4 = h_{x,1} \rho_{11} + h_{y,2} (\rho_1 - \rho_2) - 2\gamma_z \rho_4 - 2J\rho_5 + 2J\rho_7 - h_{y,1} (\rho_{10} + \rho_8) + h_{x,1} \rho_9 \tag{B13}$$

$$\partial_t \rho_5 = -h_{y,1} \rho_{11} + h_{x,2} (-\rho_1 + \rho_2) + 2J\rho_4 - 2\gamma_z \rho_5 - 2J\rho_6 + h_{x,1} (-\rho_{10} + \rho_8) + h_{y,1} \rho_9 \tag{B14}$$

$$\partial_t \rho_6 = h_{x,2} \rho_{11} + h_{y,1} (\rho_1 - \rho_3) + 2J \rho_5 - 2\gamma_z \rho_6 - 2J \rho_7 - h_{y,2} (\rho_{10} + \rho_8) - h_{x,2} \rho_9 \tag{B15}$$

$$\partial_t \rho_7 = h_{x,1}(-\rho_1 + \rho_3) - 2(J\rho_4 - J\rho_6 + \gamma_z \rho_7) + h_{x,2}(-\rho_{10} + \rho_8) - h_{y,2}(\rho_{11} + \rho_9)$$
(B16)

$$\partial_t \rho_8 = -h_{y,1} \rho_{14} + h_{x,1} \rho_{15} + h_{y,1} \rho_4 - h_{x,1} \rho_5 + h_{y,2} (-\rho_{12} + \rho_6) + h_{x,2} (\rho_{13} - \rho_7) - 4\gamma_z \rho_8 \tag{B17}$$

$$\partial_t \rho_9 = h_{x,1} \rho_{14} + h_{y,1} \rho_{15} - 2J \rho_2 + 2J \rho_3 - h_{x,1} \rho_4 - h_{y,1} \rho_5 + h_{x,2} (-\rho_{12} + \rho_6) + h_{y,2} (-\rho_{13} + \rho_7) - 4\gamma_z \rho_9$$
(B18)

$$\partial_t \rho_{10} = -4\gamma_z \rho_{10} - h_{x,2}\rho_{13} - h_{y,1}\rho_{14} - h_{x,1}\rho_{15} + h_{y,1}\rho_4 + h_{x,1}\rho_5 + h_{y,2}(-\rho_{12} + \rho_6) + h_{x,2}\rho_7 \tag{B19}$$

$$\partial_t \rho_{11} = -4\gamma_z \rho_{11} - h_{u,2}\rho_{13} + h_{x,1}\rho_{14} - h_{u,1}\rho_{15} + h_{x,1}\rho_4 + h_{u,1}\rho_5 + h_{x,2}(\rho_{12} - \rho_6) + h_{u,2}\rho_7 \tag{B20}$$

$$o_t \rho_{11} = -4 \gamma_z \rho_{11} - n_{y,2} \rho_{13} + n_{x,1} \rho_{14} - n_{y,1} \rho_{15} + n_{x,1} \rho_{4} + n_{y,1} \rho_{5} + n_{x,2} (\rho_{12} - \rho_{6}) + n_{y,2} \rho_{7}$$
(B20)

$$\partial_t \rho_{12} = -h_{x,2}\rho_{11} - 2\gamma_z \rho_{12} + 2J\rho_{13} - 2J\rho_{15} + h_{y,1}(-1 + \rho_1 + \rho_2 + \rho_3) + h_{y,2}(\rho_{10} + \rho_8) + h_{x,2}\rho_9$$

$$\partial_t \rho_{13} = h_{y,2}\rho_{11} - 2J\rho_{12} - 2\gamma_z \rho_{13} + 2J\rho_{14} - h_{x,1}(-1 + \rho_1 + \rho_2 + \rho_3) + h_{x,2}(\rho_{10} - \rho_8) + h_{y,2}\rho_9$$
(B21)

$$\partial_t \rho_{14} = -2(J\rho_{13} + \gamma_z \rho_{14} - J\rho_{15}) + h_{v,2}(-1 + \rho_1 + \rho_2 + \rho_3) + h_{v,1}(\rho_{10} + \rho_8) - h_{v,1}(\rho_{11} + \rho_9)$$
(B23)

$$\partial_t \rho_{15} = h_{y,1} \rho_{11} + 2J \rho_{12} - 2J \rho_{14} - 2\gamma_z \rho_{15} - h_{x,2} (-1 + \rho_1 + \rho_2 + \rho_3) + h_{x,1} (\rho_{10} - \rho_8) - h_{y,1} \rho_9. \tag{B24}$$

We initialize the state of the system in a product state

$$\rho(0) = \rho_1 \otimes \rho_2, \tag{B25}$$

of the individual initial qubit states $\rho_i = \frac{1}{2}(1 + \rho_x^i \sigma_x^i + \rho_y^i \sigma_y^i + \rho_z^i \sigma_z^i)$, where the vector components are sampled as $\rho_x^i, \rho_y^i, \rho_z^i \sim \mathcal{N}(0, 1)$. We consider the CNOT target transformation

$$V = \begin{pmatrix} 1 & 0 & 0 & 0 \\ 0 & 1 & 0 & 0 \\ 0 & 0 & 0 & 1 \\ 0 & 0 & 1 & 0 \end{pmatrix}, \tag{B26}$$

and the corresponding fidelity therefore reads

$$F_{\theta}(\vec{\rho}(0), \vec{\rho}(t_f)) = \text{Tr}\left(\rho_f^{\dagger} V \rho(0) V^{\dagger}\right)$$

$$= \rho_1(t_f) \rho_1(0) + 2\rho_6(t_f) \rho_{10}(0) + 2\rho_7(t_f) \rho_{11}(0) + 2\rho_8(t_f) \rho_{12}(0) + 2\rho_9(t_f) \rho_{13}(0)$$

$$+ 2\rho_{14}(t_f) \rho_{14}(0) - 2\rho_{15}(t_f) \rho_{15}(0) + \rho_2(t_f) \rho_2(0) + \rho_3(0)$$

$$- (\rho_1(t_f) + \rho_2(t_f)) \rho_3(0) - \rho_3(t_f) (-\text{Tr}(\vec{\rho}(t_f)) + \rho_1(0) + \rho_2(0) + 2\rho_3(0))$$

$$+ 2(\rho_4(t_f) \rho_4(0) + \rho_5(t_f) \rho_5(0) + \rho_{10}(t_f) \rho_6(0) + \rho_{11}(t_f) \rho_7(0) + \rho_{12}(t_f) \rho_8(0) + \rho_{13}(t_f) \rho_9(0)).$$
(B28)

Instead of evaluating this expression directly, we draw a random time $t_r \in [0, t_f]$ and propagate the initial state to that time which gives us $\rho(t_r)$. We then consider the time-local perturbation proportional to one of the accessible control operators of the Hamiltonian H_{θ} , i.e. $B_j \in \{\sigma_x^1, \sigma_x^2, \sigma_y^1, \sigma_y^2, \vec{\sigma_1} \vec{\sigma_2}\}$. In the vector representation $\vec{\rho}$, the corresponding perturbations evaluate as

$$i[\sigma_x^1, \rho] \to (-2\rho_7, -2\rho_{13}, 2\rho_7, -\rho_{11} - \rho_9, \rho_{10} - \rho_8, 0, \rho_1 - \rho_3, -\rho_{15} + \rho_5, -\rho_{14} + \rho_4, \rho_{15} - \rho_5, -\rho_{14} + \rho_4, 0, \rho_1 + 2\rho_2 + \rho_3 - 1, \rho_{11} + \rho_9, -\rho_{10} + \rho_8)^T,$$
(B29)

$$i[\sigma_x^2, \rho] \to (-2\rho_5, 2\rho_5, -2\rho_{15}, 0, \rho_1 - \rho_2, -\rho_{11} + \rho_9, \rho_{10} - \rho_8, -\rho_{13} + \rho_7, \rho_{12})$$
 (B30)

$$-\rho_6, \rho_{13}-\rho_7, -\rho_{12}+\rho_6, \rho_{11}-\rho_9, -\rho_{10}+\rho_8, 0, \rho_1+\rho_2+2\rho_3-1)^T,$$

$$i[\sigma_y^1, \rho] \to (2\rho_6, 2\rho_{12}, -2\rho_6, \rho_{10} + \rho_8, \rho_{11} - \rho_9, -\rho_1 + \rho_3, 0, \rho_{14} - \rho_4, -\rho_{15} +$$
(B31)

$$\rho_5, \rho_{14} - \rho_4, \rho_{15} - \rho_5, -\rho_1 - 2\rho_2 - \rho_3 + 1, 0, -\rho_{10} - \rho_8, -\rho_{11} + \rho_9)^T,$$

$$i[\sigma_y^2, \rho] \rightarrow (2\rho_4, -2\rho_4, 2\rho_{14}, -\rho_1 + \rho_2, 0, \rho_{10} + \rho_8, \rho_{11} + \rho_9, \rho_{12} - \rho_6, \rho_{13} - \rho_{14}, \rho_{14}, \rho_{14} + \rho_{15}, \rho_{15} + \rho_{15}, \rho_{1$$

$$\rho_7, \rho_{12} - \rho_6, \rho_{13} - \rho_7, -\rho_{10} - \rho_8, -\rho_{11} - \rho_9, -\rho_1 - \rho_2 - 2\rho_3 + 1, 0)^T,$$

$$i[\vec{\sigma_1}\vec{\sigma_2}, \rho] \to (0, -4\rho_9, 4\rho_9, 2\rho_5 - 2\rho_7, -2\rho_4 + 2\rho_6, -2\rho_5 + 2\rho_7, 2\rho_4 - 2\rho_6, 0, 2\rho_2 - \rho_3$$

$$2, 0, 0, -2\rho_{13} + 2\rho_{15}, 2\rho_{12} - 2\rho_{14}, 2\rho_{13} - 2\rho_{15}, -2\rho_{12} + 2\rho_{14})^T.$$
(B33)

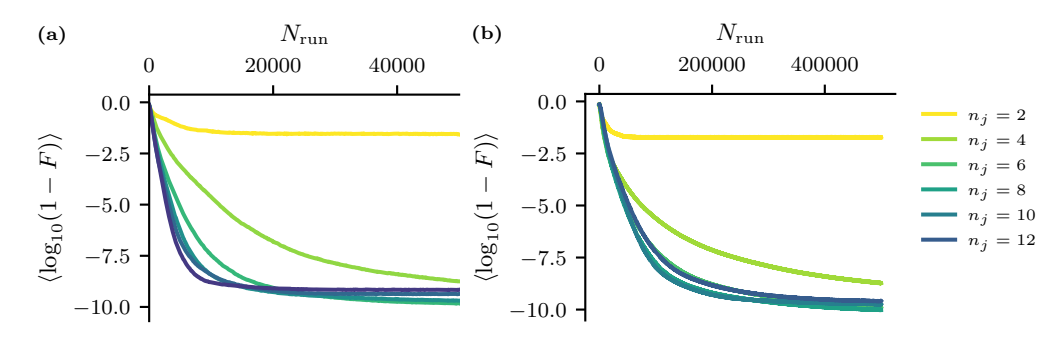


Figure 5. Number of Modes. The average infidelity $\langle \log_{10}(1-F) \rangle$, as a function of the number of runs $N_{\rm run}$, for different values of the number of modes n_j per control function. The lower bound of the infidelity is determined by the time-discretization h of the 4th-order Runge-Kutta method. Panel (a) shows the results for PEPR with a learning rate of $\alpha_{\rm PEPR} = 0.3$. Panel (b) shows the results for GRAPE with a learning rate of $\alpha_{\rm GRAPE} = 0.2$ and $\epsilon = 10^{-6}$.

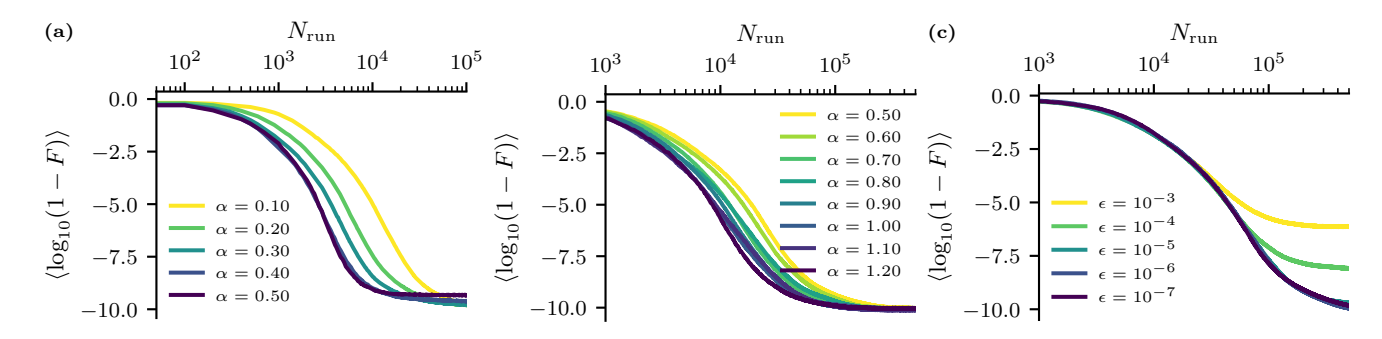


Figure 6. Hyperparameters. The average infidelity $\langle \log_{10}(1-F) \rangle$, as a function of the number of runs $N_{\rm run}$ for different values of the hyperparameters with $n_j = 8$. The lower bound of the infidelity is determined by the time-discretization h of the 4th-order Runge-Kutta method. Panel (a) shows the average infidelity based on PEPR for different values of the learning rate α . Panel (b) shows the average infidelity based on GRAPE for different values of the learning rate α . Panel (c) shows the average infidelity based on GRAPE for different values of the finite difference length ϵ .

After propagating these resulting operators from t_r to t_f , we evaluate the susceptibility of the fidelity in Eq. B28 with respect to the perturbation of B_j at time t_r , which is

$$\chi_j(t_r) = \frac{i}{\hbar} \operatorname{Tr} \left(V \rho(0) V^{\dagger} U_{\theta}(t_r, t_f) \left[B_j, U_{\theta}(t_r) \rho(0) U_{\theta}^{\dagger}(t_r) \right] U_{\theta}^{\dagger}(t_r, t_f) \right).$$
(B34)

We finally update the parameters according to PEPR as described in Eq. 15 in the main-text. It is

$$\theta_{j,k} \rightarrow \theta_{j,k} - \alpha \sin\left(\pi k \frac{t_r}{t_f}\right) \chi_j(t_r).$$
 (B35)

Note, that this update requires only a single time-evolution to obtain χ_j , which is used to update n_j -many parameters $\theta_{j,k}$. This provides better scaling with respect to the number of parameters, compared to GRAPE.

In Fig. 4 we show the average infidelity $\langle \log_{10}(1-F)\rangle$ as a function of the number of runs N_{run} for different values of γ_z , with $n_j = 8$ and $\alpha_{\text{PEPR}} = 0.4$. The average infidelity converges for $N_{\text{run}} > 10^4$ runs. Dissipation leads to a lower bound of the infidelity, which we estimate with $\gamma_z t_f$. Without dissipation, the lower bound of the infidelity is determined by the time-discretization h of the 4th-order Runge-Kutta method.

The expressibility of the control functions is determined by the number of modes n_j . In Fig. 5 we show the average infidelity $\langle \log_{10}(1-F) \rangle$ as a function of the number of runs $N_{\rm run}$ based on PEPR and GRAPE for different values of n_j . For a value of $n_j=2$, the average infidelity obtains high values, indicating insufficient expressibility of the control functions. For larger values of $n_j>2$, the average infidelity converges to a lower bound determined by numerical accuracy. We find that a value of $n_j=8$ leads to an efficient convergence behavior of the average infidelity, for both PEPR and GRAPE.

We determine an optimal set of hyperparameters of $\alpha_{PEPR} = 0.5$ for PEPR, and $\alpha_{GRAPE} = 1.2$, and $\epsilon = 10^{-7}$ for GRAPE by comparing the convergence behavior of the average infidelity Eq. 20 for different values of the hyperparameters. In Fig. 6 we show the results that motivate this particular choice of hyperparameters.

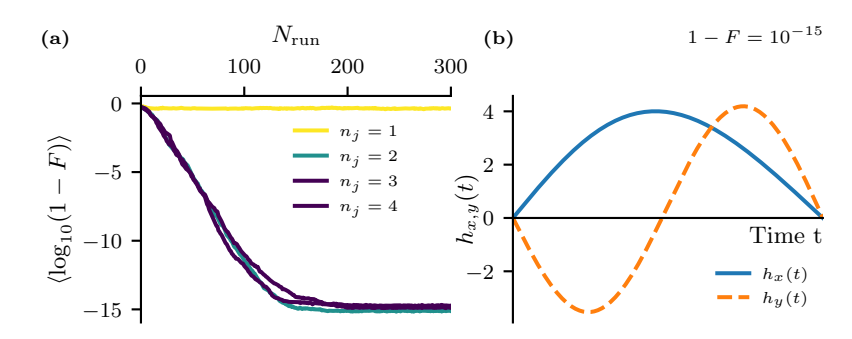


Figure 7. Results of PEPR for the Hadamard gate. Panel (a) shows the average infidelity $\langle \log_{10}(1-F) \rangle$, as a function of the number of runs N_{run} , for different values of $n_j = 1, 2, 3, 4$ and for a fixed learning rate of value $\alpha = 2.5$. The lower bound of the infidelity is determined by the time-discretization h of the 4th-order Runge-Kutta method. Panel (b) shows the control functions $h_x(t)$ and $h_y(t)$ of an example for a high-fidelity implementation for $n_j = 2$.

Appendix C: Hadamard Gate

Additionally to the optimization of the CNOT gate we demonstrate PEPR here for the example of the Hadamard gate on a single qubit. For this, we consider the Hamiltonian

$$H_{\theta}(t) = h_x(t)\sigma_x + h_y(t)\sigma_y, \tag{C1}$$

with $h_x(t) = \sum_k \theta_{x,k} \sin(\pi kt)$ and $h_y(t) = \sum_k \theta_{y,k} \sin(\pi kt)$. We write the density operator of the system as

$$\rho = \frac{1}{2} \begin{pmatrix} \xi + \rho_z & \rho_x - i\rho_y \\ \rho_x + i\rho_y & \xi - \rho_z \end{pmatrix}, \tag{C2}$$

where $\rho_i \in \mathbb{R}$, and $\xi \in \{0, 1\}$ defines the trace of the operator. We note that $\xi = 0$ is required to capture commutatorobjects such as $i[B_j, \rho]$ after the perturbation with the control operator B_j , as $\text{Tr}([B_j, \rho]) = 0$. For numerical purposes, we represent ρ as the real-valued vector

$$\vec{\rho} = (\rho_x, \rho_y, \rho_z)^T \tag{C3}$$

The dynamics of the state obey the von-Neumann equation $i\hbar\dot{\rho} = [H,\rho]$ and the equations of motion read

$$\dot{\rho}_x = 2h_y \rho_z,\tag{C4}$$

$$\dot{\rho}_y = -2h_x \rho_z,\tag{C5}$$

$$\dot{\rho}_z = 2h_x \rho_y - 2h_y \rho_x. \tag{C6}$$

We initialize the state of the system as $\vec{\rho}(0) \sim \mathcal{N}^3(0,1)$. We denote the time-propagated state over $[0,t_f]$ as $\rho(t_f)$. We consider the example of the Hadamard target transformation

$$V = \frac{1}{\sqrt{2}} \begin{pmatrix} 1 & 1\\ 1 & -1 \end{pmatrix}. \tag{C7}$$

The fidelity to reach the target state $V\rho(0)V^{\dagger}$, given the initial state $\rho(0)$, is

$$F_{\theta} = \text{Tr}(V\rho(t_0)V^{\dagger}\rho(t_f)) = \frac{1}{2}(\xi + \rho_z(t_f)\rho_x(t_0) + \rho_x(t_f)\rho_z(t_0) - \rho_y(t_f)\rho_y(t_0)). \tag{C8}$$

The control operators are $B_i \in {\sigma_x, \sigma_y}$. In the vector representation $\vec{\rho}$, the corresponding perturbations evaluate as

$$i[\sigma_x, \rho] \to (0, \rho_z, -\rho_y)^T,$$
 (C9)

$$i[\sigma_y, \rho] \to (-\rho_z, 0, \rho_x)^T.$$
 (C10)

We update the parameters according to PEPR as described in Eq. 15. It is

$$\theta_{j,k} \rightarrow \theta_{j,k} - \alpha \sin\left(\pi k \frac{t_r}{t_f}\right) \chi_j(t_r)$$
 (C11)

with the susceptibility under a randomly chosen perturbation B_j at the random time $t_r \in [0,1]$

$$\chi_j(t_r) = \frac{i}{\hbar} \operatorname{Tr} \left(V \rho(0) V^{\dagger} U_{\theta}(t_r, t_f) \left[B_j, U_{\theta}(t_r) \rho(0) U_{\theta}^{\dagger}(t_r) \right] U_{\theta}^{\dagger}(t_r, t_f) \right).$$
 (C12)

 U_{θ} denotes the unitary time-evolution operator generated by the Hamiltonian Eq. C1.

In Fig. 7 (a) we show the average infidelity $\langle \log_{10}(1-F) \rangle$, as a function of the number of runs $N_{\rm run}$ for an empirically determined optimal learning rate of $\alpha_{\rm PEPR}=2.5$. The minimal number of modes to obtain high-fidelity protocols in this simple example is $n_j>1$. The average infidelity converges to values of $\langle \log_{10}(1-F)\rangle(N_{\rm run}) \to 10^{-15}$, for $N_{\rm run}>200$. The lower bound of the infidelity is determined by the time-discretization h of the 4th-order Runge-Kutta method. We show an example for a high-fidelity implementation of the Hadamard gate with $n_j=2$ in Fig. 7 (b).